THE JOURNAL OF PHYSICAL CHEMISTRY C
A JOURNAL OF THE AMERICAN CHEMICAL SOCIETY

pubs.acs.org/JPCC

Article

Nonadiabatic Dynamics in Two-Dimensional Perovskites Assisted by Machine Learned Force Fields

Published as part of The Journal of Physical Chemistry C virtual special issue "Machine Learning in Physical Chemistry Volume 2".

David R. Graupner and Dmitri S. Kilin*

Cite This: *J. Phys. Chem. C* 2024, 128, 3935−3944

Read Online

ACCESS | Metrics & More | Article Recommendations | Supporting Information

ABSTRACT: An exploration of the "on-the-fly" nonadiabatic couplings (NACs) for nonradiative relaxation and recombination of excited states in 2D Dion−Jacobson (DJ) lead halide perovskites (LHPs) is accelerated by a machine learning approach. Specifically, ab initio molecular dynamics (AIMD) of nanostructures composed of heavy elements is performed with the use of machine-learning force-fields (MLFFs), as implemented in the Vienna Ab initio Simulation Package (VASP). The force field parametrization is established using on-the-fly learning, which continuously builds a force field using AIMD data. At each time step of the molecular dynamics (MD) simulation, the total energy and forces are predicted based on the MLFF and if the Bayesian error estimate exceeds a threshold, an ab initio calculation is performed, which is used to construct a new force field. Model training of MLFF and evaluation were performed for a range of DJ-LHP models of different thicknesses and halide compositions. The MLFF-MD trajectories were evaluated against pure AIMD trajectories to assess the level of discrepancy and error accumulation. To examine the practical effectiveness of this approach, we have used the MLFF-based MD trajectories to compute NAC and excited-state dynamics. At each stage, results based on machine learning are compared to traditional ab initio based electronic dissipative dynamics. We find that MLFF-MD provides comparable results to AIMDs when MLFF is trained in an *NPT* ensemble.

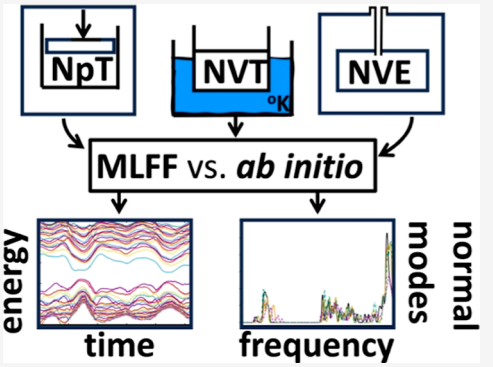

1. INTRODUCTION

A popular candidate for next-generation optoelectronic devices are thin-film $CsPbX_3$ (X = Cl, Br, and I) lead halide perovskites (LHPs) due to their increased stability when compared to the bulk LHPs[1] and favorable optoelectronic properties.[2−11] The stability of the two-dimensional (2D) perovskites is dictated by their confinement regime,[12] where variations of layer thickness are expected to have a qualitatively similar degree of stability, while being away from the three-dimensional (3D) bulk regime. The insulating qualities of the organic molecules in the structure result in the thin-film perovskite structures possessing natural quantum-well structures[13] which induce both the quantum confinement and dielectric effects.[14] 2D LHPs are categorized by the thickness of the perovskite layer (*n* perovskite octahedra) and the relative stacking of the perovskite layers, with the Ruddlesden−Popper (RP) phase[15] and Dion−Jacobson (DJ) phase[16,17] being the most common structures studied. The RP perovskites show an offset of (1/2,1/2) between perovskite layers due to the divalent organic spacers, while the DJ perovskites exhibit an offset of (0,0).

Ab initio molecular dynamics (AIMD) are used to determine how atoms move over time, but AIMD is computational demanding which imposes limits on the size of models studied.[18−21] One potential way to address this problem is by combining AIMD simulations and machine learning to generate machine learned force fields (MLFFs).[22,23] Large and accurate data sets are used to construct traditional MLFFs; therefore, there is a lot of trial and error involved in parameter optimization and data selection.[24] Generating on-the-fly MLFF through active learning schemes gives the advantage that no prior training is required and the on-the-fly force fields are generated automatically during the AIMD simulation.[25,26] Using this approach, the results can be achieved with the accuracy of AIMD while also speeding up the simulation.[22] The on-the-fly MLFF approach enables the extension of simulation scales in both size and time, thereby making it possible to unveil new phenomena previously not possible with only ab initio methods.

Received: October 31, 2023
Revised: January 15, 2024
Accepted: January 24, 2024
Published: February 22, 2024

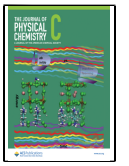

Methodology that goes beyond the Born−Oppenheimer approximation (BOA) is required to computationally model excited-state processes, such as nonradiative relaxation and photoluminescence.[27] The BOA separates electronic and nuclear degrees of freedom and does not allow for energy flow between them. However, there are a range of processes in excited states that are related to energy transfer between nuclear degrees of freedom and electronic degrees of freedom. Computing nonadiabatic couplings (NACs) is one of the most common approaches for accomplishing this. NACs can be computed by using a molecular dynamics (MD)-based "on-the-fly" approach[28] or with normal-mode analysis by explicitly solving for eigenfrequencies and eigenmodes.[29] NACs can then be used to describe the dynamics of electronic states using several computational approaches, such as Tully's surface hopping procedure[30] and reduced density matrix (RDM) implemented in the multilevel Redfield theory.[31−35]

Here, we report the effects of using MLFF on excited-state dynamics and normal modes of vibration. Excited-state dynamics are used to characterize the PL properties and are calculated from the computed NACs between nuclear and electronic degrees of freedom from adiabatic MD trajectories. The reduced density matrix formalism within Redfield theory from the NACs.[36,37] The models examined in this paper are DJ cesium lead halide perovskites with n = 1, 2, 3, and 5, with 1,4-butyldiammonium as the linker molecule separating perovskite layers. Mean squared displacement (MSD) is used to compare AIMD trajectories to MLFF-MD trajectories. Excited-state dynamics results based on pure AIMD and MLFF-MD are empirically compared to view the effects that MLFF has on the radiative and nonradiative properties and to determine under which conditions the use of MLFF-MD fails to reproduce the AIMD results. Using MLFF trained using a MD calculation under the isothermal−isobaric ensemble is expected to provide the most comparable results to those provided by AIMD.

2. METHODS

2.1. Ground-State Electronic Structure Calculations.

Noncollinear spin DFT[38,39] is used as the electronic basis, and due to the large angular momentum of conduction band Pb^{2+} 6p orbitals, we include the SOC interaction. A self-consistent noncollinear spin DFT uses four densities $\rho_{\sigma\sigma'}(\vec{r})$ and rests on the Kohn−Sham (KS) equation

$$\sum_{i,\sigma'=\alpha,\beta} (-\delta_{\sigma\sigma'}\nabla^2 + v^{\text{eff}}_{\sigma\sigma'}[\rho_{\sigma\sigma'}(\vec{r})])\varphi_{i\sigma}(\vec{r}) = \varepsilon_i\varphi_{i\sigma'}(\vec{r}) \tag{1}$$

where $v^{\text{eff}}_{\sigma\sigma'}\rho_{\sigma\sigma'}(\vec{r})$ is the 2 × 2 matrix operator of effective potential and α and β are orthogonal spin indices. In accordance with the self-consistent Kohn−Sham theorem, the 2 × 2 effective potential is a functional of the electronic density for a N electron system $v^{\text{eff}}_{\sigma\sigma'} = \frac{\delta E^{\text{TOT}}[\rho^N_{\sigma\sigma'}]}{\delta\rho^N_{\sigma\sigma'}}$

Spinor Kohn−Sham orbitals (SKSOs), which are two-component wave functions composed of a superposition of $|\alpha\rangle$ and $|\beta\rangle$ spin components, result from solutions of eq 1.

$$\varphi^{\text{SKSO}}_i(\vec{r}) = \begin{Bmatrix}\varphi_{i\alpha}(\vec{r})\\ \varphi_{i\beta}(\vec{r})\end{Bmatrix} = \varphi_{i\alpha}(\vec{r})|\alpha\rangle + \varphi_{i\beta}(\vec{r})|\beta\rangle \tag{2}$$

Within the noncollinear spin DFT framework, relativistic effects can be incorporated by using second-order scalar relativistic corrections.

$$H^{\text{relativistic}} = H^{\text{SR}} + H^{\text{SOC}} \tag{3}$$

H^{SOC} is the SOC term and H^{SR} is the scalar relativistic term. The H^{SOC} describes energy shifts of spin occupations and the H^{SR} term describes relativistic kinetic energy corrections. Up to the second order, H^{SOC} is represented as

$$H^{\text{SOC}} = \frac{\hbar}{4m^2c^2}\frac{1}{r}\frac{\partial\nu^{\text{KS}}_{\text{sphere}}}{\partial r}\vec{L}\cdot\vec{S} \tag{4}$$

where $\vec{S}$ is composed of Pauli spin matrices and $\vec{L}$ is the angular momentum operator.

We use the independent orbital approximation (IOA)[40,41] in which excited states are described as a pair of orbitals, as opposed to a superposition of orbitals commonly used in TDDFT or Bethe-Saltpeter approaches. Oscillator strengths, eq 5, between SKSOs i and j can be computed using transition dipole matrix elements, eq 6.

$$f_{ij} = |\vec{D}_{ij}|^2\frac{4\pi m_e\nu_{ij}}{3\hbar e^2} \tag{5}$$

$$\langle\vec{D}_{ij}\rangle = e\int d\vec{r}\{\varphi^*_{i\alpha} \quad \varphi^*_{i\beta}\}\vec{r}\begin{Bmatrix}\varphi_{j\alpha}\\ \varphi_{j\beta}\end{Bmatrix} \tag{6}$$

where ν_{ij} represents the transition frequency between SKSO i and j. The transition frequency ν_{ij} is related to the transition energy ΔE_{ij} by the equation $h\nu_{ij} = \Delta E_{ij}$.

Normal modes of vibration where found from determining the Hessian matrix

$$H_{IJ} = \frac{\partial^2 V([\hat{\rho}])}{\partial R_I\partial R_J} \tag{7}$$

where $V([\hat{\rho}])$ is the electronic potential as a functional of the electronic density ρ and R_I represents the Cartesian projections of spatial coordinates. From the Hessian equation, an eigenvalue equation can be solved to determine the eigenmodes and eigenfrequencies of ionic motion. The density of normal modes (vDOS) is computed as.

$$\nu\text{DOS} = \sum_I \delta(\nu - \nu^{\text{NM}}_I) \tag{8}$$

where ν^{NM}_I is the energy of the eigenfrequency of ionic motion. Thermal broadening is approximated as a Gaussian. Comparison of the normal modes of vibration calculated using ab initio methods and the MLFF is done using root-mean-square error.

$$\text{RMSE} = \sqrt{\frac{1}{n}\sum_{I=1}^{n}(\nu\text{DOS}^{\text{Ab}}_{\nu_I} - \nu\text{DOS}^{\text{ML}}_{\nu_I})^2} \tag{9}$$

where n is the total number of eigenfrequencies of ionic motion, ν_I is the eigenfrequency of ionic motion, $\text{vDOS}^{\text{Ab}}_{\nu_I}$ is the density of vibrational modes for the ab initio calculation, and $\nu\text{DOS}^{\text{ML}}_{\nu_I}$ is the density of vibrational modes energy for the MLFF calculation.

Adiabatic molecular dynamics (MD) is used to dynamically couple nuclear and electronic degrees of freedom. This provides kinetic energy of nuclei to break the orthogonality of electronic states. The nuclear degrees of freedom are treated in the classical path approximation (CPA) with the nuclei

https://doi.org/10.1021/acs.jpcc.3c07216
J. Phys. Chem. C 2024, 128, 3935−3944

following classical path trajectories. The initial velocities of nuclei are scaled to keep a constant temperature, eq 10

$$\sum_{I=1}^{N^{\text{ion}}} \frac{M_{\text{I}}}{2}\left(\frac{\mathrm{d}\vec{R}_{\text{I}}}{\mathrm{d}t}|_{t=0}\right)^2 = \frac{3}{2}N^{\text{ion}}k_{\text{B}}T \tag{10}$$

where T is the temperature, k_{B} is the Boltzmann constant, M_{I} is mass of the I^{th} nuclei, and $\vec{R}_{\text{I}}$ represents ionic coordinates. The forces acting on the nuclei depending on the

$$\frac{\mathrm{d}^2}{\mathrm{d}t^2}\vec{R}_{\text{I}} = \vec{F}_{\text{I}}(\hat{\rho}^N_{\sigma\sigma'})/M_{\text{I}} \tag{11}$$

where $\vec{F}_{\text{I}}([\hat{\rho}])$ is the force acting on the ions is a functional of the electronic density.

2.2. Machine Learned Force Field. To describe the atomic interaction potential, the MLFF scheme utilized a potential energy description method[24] similar to smooth overlap of atomic positions (SOAP)[42] and Gaussian approximation potential (GAP).[43] The potential energy, U, was approximated as the sum of the local energies, U_i, for structures containing N_{a} atoms.

$$U = \sum_{i=1}^{N_{\text{a}}} U_i = \sum_{i=1}^{N_{\text{a}}}\sum_{i_{\text{B}}}^{N_{\text{B}}} w_{i_{\text{B}}} K(\boldsymbol{X}_i, \boldsymbol{X}_{i_{\text{B}}}) \tag{12}$$

where $w_{i_{\text{B}}}$ is weight factors, N_{B} is the number of local reference structures, and the kernel function, $K(\boldsymbol{X}_i, \boldsymbol{X}_{i_{\text{B}}})$, which evaluates the similarity between the local configuration around atom i and the reference local configuration i_{B}. The parameters and form of the atomic interaction potential function was determined using Bayesian linear regression, while providing estimates of confidence intervals to evaluate the reliability of the fitting results. Angular functions and distribution functions are combined as descriptors to represent the local chemical environment by the algorithm.[44] Here, the initial threshold was set to 0.002 eV/Å and each MLFF was determined using approximately 800 local reference structures. The structure and corresponding local configuration were trained when the force error of any atom exceeded the threshold.

2.3. Reduced Density Matrix Equation of Motion for Electronic Degrees of Freedom. To describe the time evolution of electronic degrees of freedom that are weakly coupled to a thermal bath the Redfield quantum master equation[35,45] in the density matrix formalism is used. The Markov approximation is assumed in the typical implementation of the Redfield approach, where the model is immersed into a heat bath so that the bath temperature is constant as the bath is infinitely larger than the model of explicit interest.

$$\frac{\mathrm{d}}{\mathrm{d}t}\hat{\rho} = -\frac{i}{\hbar}\sum_k (F_{ik}\rho_{kj} - \rho_{ik}F_{kj}) + \left(\frac{\mathrm{d}\rho_{ij}}{\mathrm{d}t}\right)_{\text{diss}} \tag{13}$$

where ρ is the density matrix and F is the many-electron Fock matrix, which includes exchange and correlation. The unitary time evolution of a closed system is described in the first term using the Liouville−von Neumann equation. While the second term describes electronic energy dissipation due to weak coupling to a thermal bath. NACs computed "on-the-fly" in the basis of SKSOs is used to parametrize the dissipative transitions

$$\begin{aligned}\hat{V}^{\text{NA}}_{ij}(t) &= -i\hbar\left\langle \varphi_i^{\text{SKSO}}(\vec{r}, \{\vec{R}_{\text{I}}(t)\})\middle|\frac{\partial}{\partial t}\middle|\varphi_j^{\text{SKSO}}(\vec{r}, \{\vec{R}_{\text{I}}(t)\})\right\rangle \\ &= -\frac{i\hbar}{2\Delta t}\int \mathrm{d}\vec{r}\{\varphi^*_{i\alpha}(\vec{r}, \{\vec{R}_{\text{I}}(t)\}) \\ &\quad \varphi^*_{i\beta}(\vec{r}, \{\vec{R}_{\text{I}}(t)\})\}\cdot\begin{Bmatrix}\varphi_{j\alpha}(\vec{r}, \{\vec{R}_I(t+\Delta t)\}) \\ \varphi_{j\beta}(\vec{r}, \{\vec{R}_{\text{I}}(t+\Delta t)\})\end{Bmatrix} + h.\,c.\end{aligned} \tag{14}$$

The orthogonality relation is broken and provides a "mixing" of SKSOs due to the nuclear kinetic energy of nuclei. The Fourier transform of the autocorrelation function is used to convert NACs into rates of transitions

$$M_{ijkl}(\tau) = \frac{1}{T}\int_0^T V^{\text{NA}}_{ij}(t+\tau)V^{\text{NA}}_{kl}(t)\mathrm{d}t \tag{15a}$$

$$\Gamma^+_{ijkl} = \frac{1}{T}\int_0^T M_{ijkl}(\tau)\mathrm{e}^{-i\omega_{ij}\tau}\mathrm{d}\tau \tag{15b}$$

$$\Gamma^-_{ijkl} = \frac{1}{T}\int_0^T M_{ijkl}(\tau)\mathrm{e}^{-i\omega_{kl}\tau}\mathrm{d}\tau \tag{15c}$$

which provides components for the Redfield tensor, eq 16.

$$R_{ijkl} = \Gamma^+_{ljik} + \Gamma^-_{kjil} + \delta_{jl}\sum_m \Gamma^+_{immk} - \delta_{ik}\sum_m \Gamma^-_{jmml} \tag{16}$$

The dissipative dynamics of the density matrix are controlled by the Redfield tensor.

$$\left(\frac{d\rho_{ij}}{\mathrm{d}t}\right)_{\text{diss}} = \sum_{lm} R_{ijlm}\rho_{lm} \tag{17}$$

From the Redfield tensor R_{ijkl}, we can approximate a nonradiative recombination rate k_{nr} from Redfield matrix elements.

$$k_{\text{nr}} \approx R_{\text{HO-LU}} \tag{18}$$

2.4. Excited-State Observables. Along the excited-state trajectory, we can compute time-resolved observables such as changes in charge carrier occupations, eqs 19a and 19b

$$n^{(a,b)}(\varepsilon, t) = \sum_i \rho^{(a,b)}_{ii}(t)\delta(\varepsilon - \varepsilon_i) \tag{19a}$$

$$\Delta n^{(a,b)}(\varepsilon, t) = n^{(a,b)}(\varepsilon, t) - n^{\text{eq}}(\varepsilon, t) \tag{19b}$$

and average charge carrier energy, eq 20a and eq 20b.

$$\langle \Delta\varepsilon_{\text{e}}(t)\rangle = \sum_{i\geq \text{LU}} \rho_{ii}(t)\varepsilon_i(t) \tag{20a}$$

$$\langle \Delta\varepsilon_{\text{h}}(t)\rangle = \sum_{i\leq \text{HO}} \rho_{ii}(t)\varepsilon_i(t) \tag{20b}$$

To get the rates of charge carrier relaxation to band edges, we convert the energy expectation value from eq 20a and eq 20b into dimensionless energy, eq 21. We fit eq 21 to an exponential decay, assuming a single exponential decay

$$\langle E_{\text{e/h}}\rangle(t) = \frac{\langle \Delta E_{\text{e/h}}\rangle(t) - \langle \Delta E_{\text{e/h}}\rangle(\infty)}{\langle \Delta E_{\text{e/h}}\rangle(0) - \langle \Delta E_{\text{e/h}}\rangle(\infty)} \tag{21}$$

and solve for the rate constant $k_{\text{e/h}}$, eq 22.

$$k_{\text{e/h}} = \{\tau_{\text{e/h}}\}^{-1} = \{\int_0^\infty \langle E_{\text{e/h}}\rangle(t)\mathrm{d}t\}^{-1} \tag{22}$$

https://doi.org/10.1021/acs.jpcc.3c07216
J. Phys. Chem. C 2024, 128, 3935−3944

Rates of radiative recombination k_r can be found from Einstein coefficients for spontaneous emission[46]

$$k_r = A_{HO-LU} = \frac{8\pi^2 \nu_{HO-LU}^2 e^2}{\varepsilon_0 m_e c^3} \frac{g_I}{g_J} f_{HO-LU} \quad (23)$$

f_{HO-LU} is the oscillator strength, ν_{HO-LU}^2 represents the transition frequency for the HO−LU transition where i = HO and j = LU, g_I is the degeneracy of the Ith electronic state, and the rest of the variables represent the fundamental constants. From the radiative and nonradiative recombination rates k_r and k_{nr}, we compute a PLQY.

$$PLQY = \frac{k_r}{k_r + k_{nr}} \quad (24)$$

2.5. Computational and Atomistic Details. The periodic model is created from the bulk $CsPbX_3$ (X = Cl, Br, and I) crystal structure, $2 \times 2 \times n$ unit cells were carved out, n = 1, 2, 3, or 5, giving three X/Cs terminated surfaces and three Pb/X terminated surfaces providing a composition of Cs_{4n} Pb_{4n} X_{12n}.[47,48] The Cs atoms are removed from the 2 × 2 unit cell X/Cs terminated surface and replaced with 1,4-butanediammonium (BdA) molecules. X atoms are then added on the opposite ends of the BdA molecules, in line with the octahedral Pb/X structures from the initial crystal structure. Overall, this gives a structure of $BdA_4Cs_{4(n-1)}$ Pb_{4n} X_{16n}. Here, we explore the n = 2 and n = 5 $PbCl_3$, n = 1 and 2 $PbBr_3$, and n = 3 PbI_3 DJ LHPs with the geometry of the models illustrated in Figure S1.

DFT in a plane-wave basis set along with projector augmented-wave (PAW) pseudopotentials[49,50] with the generalized gradient approximation (GGA) Perdew−Burke−Ernzerhof (PBE) functional[51] in Vienna Ab initio Simulation Package (VASP)[52] software was used to calculate the ground-state electronic structure of our atomistic model. Observables were computed using subsequent single point calculations performed using noncollinear spin DFT including the SOC interaction for all systems. All calculations were performed at the Γ point.

To initialize MD, the models were set to a Nose−Hoover thermostat[53] and heated to 300 K and 500 K for n = 2 $PbCl_3$ model. Once temperature was reached, the MD trajectory was propagated for 1 ps using Δt = 1 fs time steps under the *NVE* ensemble. The MD calculations was performed using ab initio methodology and using the MLFF. MSD is used to compare the results of the MLFF-MD and AIMD trajectories.

$$MSD(t) = \frac{1}{N} \sum_{I=1}^{N} |\vec{R}_I^{Ab}(t) - \vec{R}_I^{ML}(t)|^2 \quad (25)$$

where N is the number of atoms, $\vec{R}_I^{Ab}(t)$ is the ionic coordinates of the AIMD trajectory at time t, and $\vec{R}_I^{ML}(t)$ is the ionic coordinates of the MLFF-MD trajectory at time t. The MLFF-MD calculations were performed under the conditions: (i) using the model that was heated using the ab initio Nose−Hoover thermostat before using the MLFF to simulate the MD trajectory under the *NVE* ensemble and (ii) using the MLFF to simulate the Nose−Hoover thermostat heating and the MD trajectory under the *NVE* ensemble. These methods will be referred to as MLFF-MD method A and MLFF-MD method B, respectively. To determine the effect on the excited-states dynamics, three MLFFs were generated by performing the training using MD calculations performed on isothermal−isobaric (*NPT*), canonical (*NVT*), and microcanonical (*NVE*) ensembles. All three MLFFs were trained using a n = 1 $PbBr_3$, n = 2 $PbCl_3$, and n = 3 PbI_3 DJ LHP and each trajectory was allowed to propagate for 2000 timesteps for each of the models used to train the MLFFs. *NPT* and *NVT* training calculations used temperature ramping from 0 to 800 K, while *NVE* training calculations were performed at 300 K. Results determined for MD calculations performed using the MLFF trained on the *NPT*, *NVT*, and *NVE* ensembles will be referred to as scheme 1, scheme 2, and scheme 3, respectively. The abbreviations and descriptions of the MLFF-MD methods and MLFF training schemes used is described in Table 1. NACs are then computed using an "on-the-fly' procedure along a nuclear trajectory, from AIMD or MLFF-MD, where $\hat{V}_{ij}^{NA}(t) \approx \langle \varphi_i \left| \frac{d}{dt} \right| \varphi_j \rangle$.

Table 1. Abbreviation and Description of Methods Used to Train MLFF and Perform *NVE* MD

method abbreviation	description
MLFF-MD method A	MLFF-MD technique was used to compute the *NVE* MD simulation using the models that were heated using the ab initio Nose−Hoover thermostat
MLFF-MD method B	MLFF-MD technique was used to compute both the Nose−Hoover thermostat heating and *NVE* MD simulation
scheme 1	MLFF was generated by training in a *NPT* ensemble
scheme 2	MLFF was generated by training in a *NVT* ensemble
scheme 3	MLFF was generated by training in a *NVE* ensemble

3. RESULTS

Figure 1 shows the temperature for the *NVE* MD simulations where (a−d) the MLFF-MD method A and (e−h) the MLFF-MD method B were used with (a,e) n = 2 $PbBr_3$, (b,f) n = 2 $PbCl_3$, (c,g) n = 3 PbI_3, and (d,h) n = 5 $PbCl_3$ perovskite models. For each plot in Figure 1, the temperature is plotted for the ab initio (black, solid), scheme 1 (orange, solid), scheme 2 (purple, dot-dash), and scheme 3 (green, dot-dot-dash−dash) calculations. For all models, it is observed that the temperature for scheme 2 quickly rises to values greater than 10,000 K, as illustrated in Figure S2. Scheme 1 shows an increase in temperature for all models and MLFF-MD methodologies when compared to the ab initio calculations except for MLFF-MD method B for both $PbCl_3$ models. Scheme 3 exhibits temperatures that vary slightly from the ab initio calculations except for the $PbBr_3$ models.

The MSD of the MD trajectories is shown in Figure 2 using (a−d) the MLFF-MD method A and (e−h) the MLFF-MD method B with (a,e) n = 2 $PbBr_3$, (b,f) n = 2 $PbCl_3$, (c,g) n = 3 PbI_3, and (d,h) n = 5 $PbCl_3$ perovskite models. For each plot in Figure 2, the MSD is determined for the *NVE* MD calculation and plotted for scheme 1 (orange, solid), scheme 2 (purple, dot-dash), and scheme 3 (green, dot-dot-dash-dash) calculations. For Figure 2e−h, the MSD is determined for the Nose−Hoover thermostat heating and plotted for scheme 1 (red, solid), scheme 2 (blue, dot-dash), and scheme 3 (black, dot-dot-dash-dash) calculations. The gray line represents the level of error that is indicative of a temperature increase when compared to the ab initio as shown in Figure 1. It is seen that the MSD for scheme 2 crosses the error line within 300 fs of the beginning of the *NVE* MD calculation. Scheme 1 and scheme 3 show similar results during the beginning of the *NVE*

https://doi.org/10.1021/acs.jpcc.3c07216
J. Phys. Chem. C 2024, 128, 3935−3944

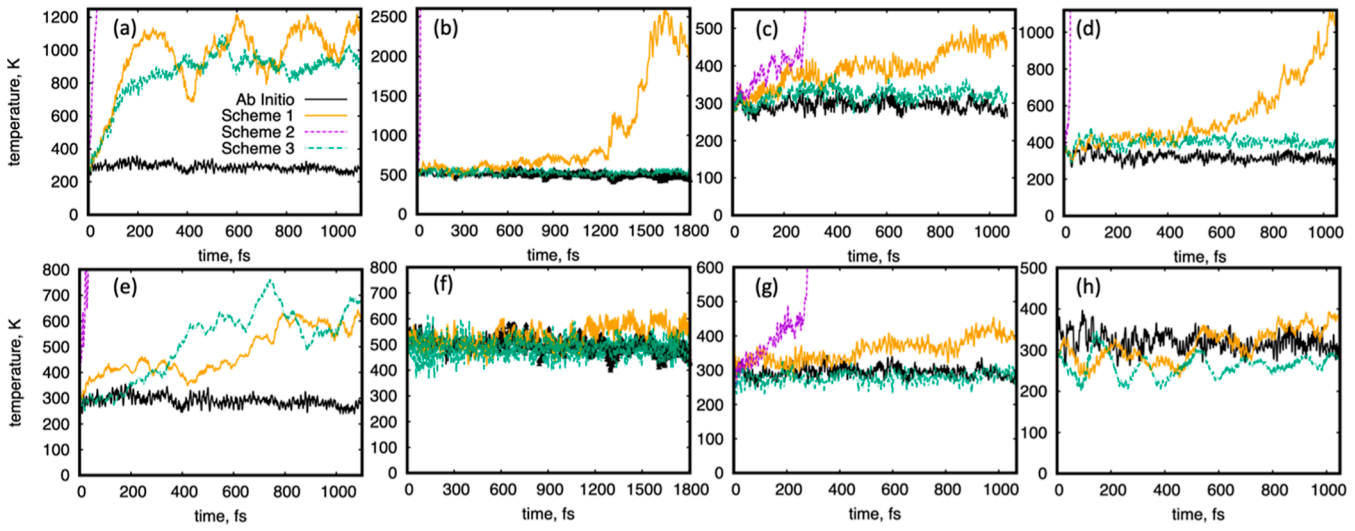

Figure 1. Calculated temperatures of the *NVE* MD simulations for (a−d) MLFF-MD method A and (e−h) MLFF-MD method B, where (a,e) are n = 2 $PbBr_3$, (b,f) are n = 2 $PbCl_3$, (c,g) are n = 3 PbI_3, and (d,h) are n = 5 $PbCl_3$ perovskite models. For all panels, the temperature is plotted for the ab initio (black, solid), scheme 1 (orange, solid), scheme 2 (purple, dot-dash), and scheme 3 (green, dot-dot-dash-dash) calculations. In all calculations, the temperature for the scheme 2 calculations increases to values larger than 15,000 K within 400 fs.

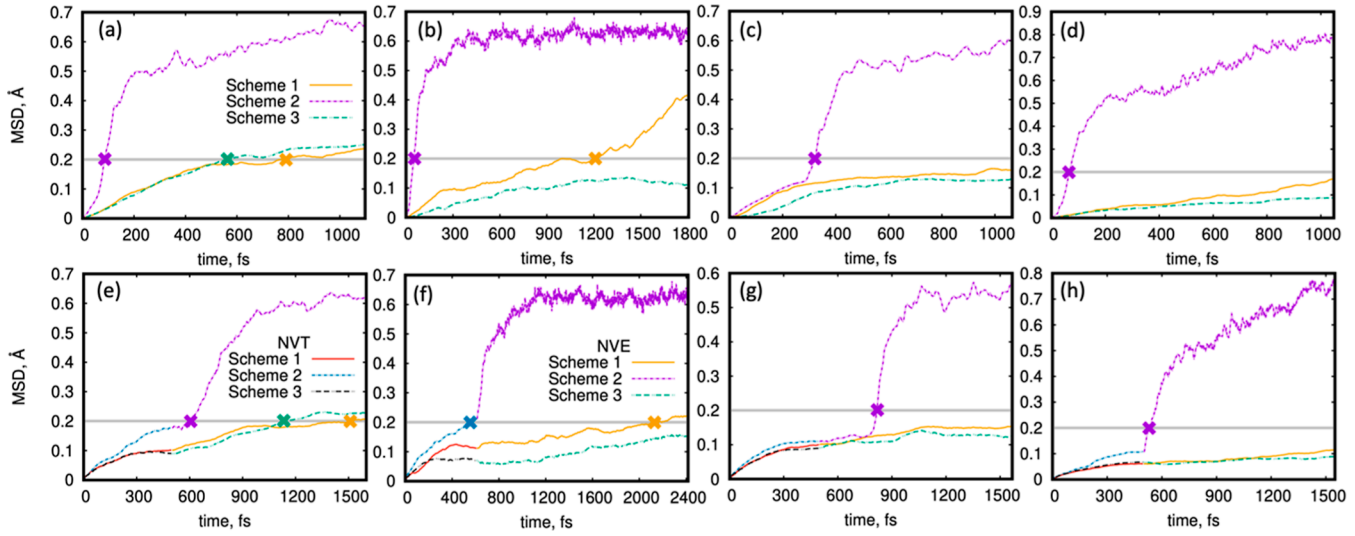

Figure 2. MSD of the MD trajectories for (a−d) MLFF-MD method A and (e−h) MLFF-MD method B, where (a,e) are n = 2 $PbBr_3$, (b,f) are n = 2 $PbCl_3$, (c,g) are n = 3 PbI_3, and (d,h) are n = 5 $PbCl_3$ perovskite models. For panels (e−h), the MSD is determined for the Nose−Hoover thermostat heating and plotted for scheme 1 (red, solid), scheme 2 (blue, dot-dash), and scheme 3 (black, dot-dot-dash-dash) calculations. For all panels, the MSD is determined for the *NVE* MD simulation and plotted for scheme 1 (orange, solid), scheme 2 (purple, dot-dash), and scheme 3 (green, dot-dot-dash-dash) calculations. The gray line represents the level of error that is indicative of a temperature increase when compared to the ab initio as shown in Figure 1. The X-marks indicate when a MSD value for a specific scheme crosses the gray line, the colors correspond to the colors used by the scheme that crosses the error line.

MD calculation but the scheme 3 calculation tends to increase in MSD as we approach the end of the simulation. For the $PbBr_3$ model, both scheme 1 and scheme 3 cross the error line at approximately 600 and 800 fs into the *NVE* MD simulations, respectively.

The response of electronic energies to the thermalization of the model is shown as energy fluctuations of the SKSO in Figure 3 for the n = 5 $PbCl_3$ model using (a) ab initio and MLFF-MD method B (b) scheme 1, (c) scheme 2, and (d) scheme 3 calculations. The ab initio calculation shows relatively consistent energy fluctuations throughout the duration of *NVE* MD simulation. The scheme 3 calculation exhibits the greatest similarity to the energy fluctuations of the ab initio calculation; however, it is observed that the gap decreases as the simulation occurs and due to an increase of sub gaps between 200 and 400 fs. SKSO energy fluctuation for the scheme 1 calculations shows an oscillation, greater than 0.5 eV, approximately every 200 fs, resulting in several periods where the gap is smaller than in scheme 3 and other periods where the gap is similar. At approximately 900 fs, a subgap forms in the valence band and closes the gap. The SKSO energy fluctuations for the scheme 2 calculations shows a closed gap throughout the simulation and quickly changing energy values due to the large temperature resulting from these calculations. SKSO energy fluctuations for the other perovskite models and MLFF-MD method A are illustrated in Figures

https://doi.org/10.1021/acs.jpcc.3c07216
J. Phys. Chem. C 2024, 128, 3935−3944

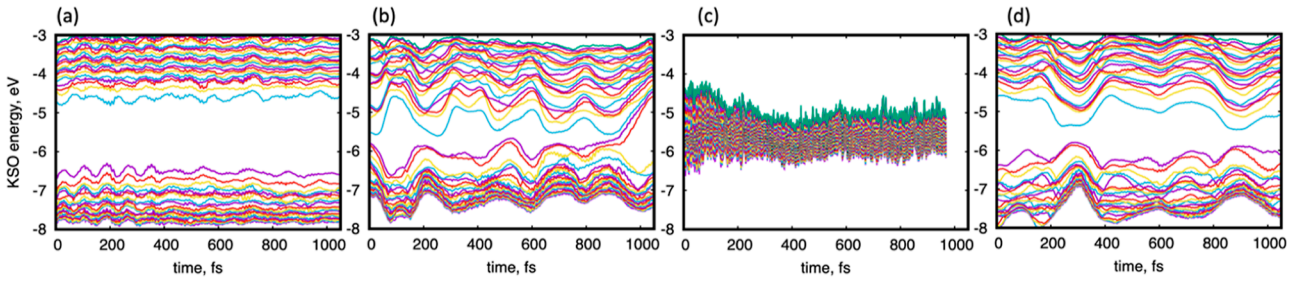

Figure 3. SKSO energy fluctuations along the *NVE* MD trajectory for the n = 5 $PbCl_3$ perovskite model using MLFF-MD method B. (a) Ab initio, (b) scheme 1, (c) scheme 2, and (d) scheme 3 methodologies were used to calculate the *NVE* MD trajectory. Each color represents a band energy for a SKSO along the MD trajectory which fluctuate due thermal motion of ions. SKSO energy fluctuations for MLFF-MD method A and the other perovskite models is shown in Figures S3−S6.

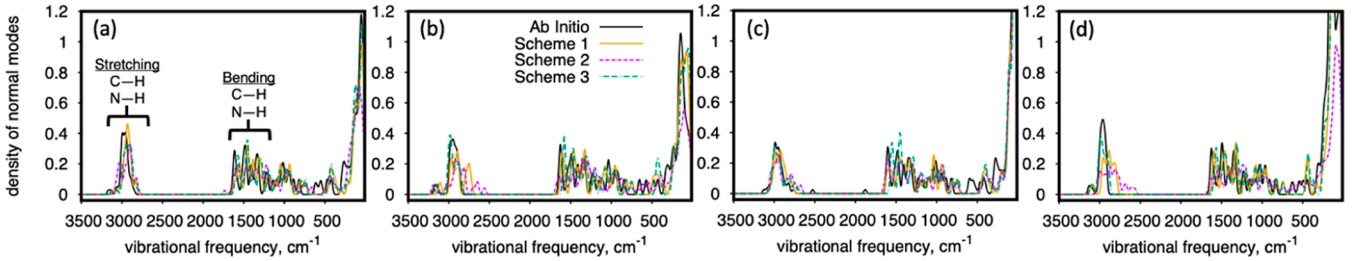

Figure 4. Normal modes of vibration calculated with ab initio (black, solid), scheme 1 (orange, solid), scheme 2 (purple, dot-dash), and scheme 3 (green, dot-dot-dash-dash) calculations for (a) n = 2 $PbBr_3$, (b) n = 2 $PbCl_3$, (c) n = 3 PbI_3, and (d) n = 5 $PbCl_3$ perovskite models. It is observed that there is good qualitative agreement between the methods used for the n = 2 $PbBr_3$ and n = 3 PbI_3 models. The n = 2 $PbCl_3$ and n = 5 $PbCl_3$ models show good qualitative agreement in all regions except between 3000 and 2500 cm^{-1}.

S3−S6 and exhibit similar trends to the results for n = 5 $PbCl_3$ MLFF-MD method B except for the $PbBr_3$ model scheme 3 calculations also show a subgap forming in the valence band at approximately 300 fs that closes the gap in a similar manner as is observed for the scheme 1 calculation in Figure 3b.

Figure 4 shows the vibrational modes in the ground state for the (a) n = 2 $PbBr_3$, (b) n = 2 $PbCl_3$, (c) n = 3 PbI_3, and (d) n = 5 $PbCl_3$ models calculated using ab initio (black, solid), scheme 1 (orange, solid), scheme 2 (purple, dot-dash), and scheme 3 (green, dot-dot-dash-dash) calculations. The peaks near 3000 and 1500 cm^{-1} are attributed to features in the BdA linker molecules. The vibrational modes for all calculations show qualitative agreement below 2500 cm^{-1} but the $PbCl_3$ models exhibit additional vibrational modes between 3000 and 2500 cm^{-1}. The RMSE was calculated for the vibrational modes calculated using the MLFFs against the vibrational modes calculated using ab initio calculations, as shown in Table 2. It is shown that the RMSE is less than 0.1 for all models and MLFF schemes except for the n = 5 $PbCl_3$, which exhibits an RMSE of less than 0.2 for all MLFF schemes.

The Redfield tensor, which represent the rates of state-to-state transitions in units of ps^{-1} and are used to calculate the nonradiative dissipation, is shown in Figure 5 for n = 3 PbI_3 (a) ab initio and (b) MLFF-MD method B scheme 1 calculations.

Table 2. RSME Calculated for the Normal Modes of Vibration Using eq 9

model	scheme 1	scheme 2	scheme 3
n = 2 $PbBr_3$	0.06374	0.07466	0.06815
n = 2 $PbCl_3$	0.07269	0.08136	0.09009
n = 3 PbI_3	0.07793	0.07147	0.09588
n = 5 $PbCl_3$	0.16178	0.19073	0.14130

In both cases, it is observed that there are alternating high intensity transitions between near-degenerate states near the main diagonal. Figure 5c shows the relative difference between the Redfield tensor calculated by using AIMD and MLFF-MD. Table 3 shows the rate of electron and hole energy dissipation determined by nonadiabatic dynamics. The initial condition shown is the transition with the highest oscillator strength that does not involve one of the near-degenerate principal band gap orbitals; Table S2 shows values for rates for the second and third highest oscillator strengths that do not involve one of the near-degenerate principal band gap orbitals. Calculations performed using scheme 2 showed rates that were an order of magnitude larger than those obtained from the ab initio calculations. The energy dissipation rates for schemes 1 and 3 show results that tend to be on the same order of magnitude as the rates for the ab initio calculations. Rates calculated using the MLFF-MD method B trajectories tend to overestimate the values calculated using the ab initio calculation, while the rates calculated with the MLFF-MD method A trajectories tend to both over and underestimate values. Table 4 shows the HO−LU transition oscillator strength, radiative and nonradiative recombination rate, and PLQY calculated by using the nonadiabatic dynamics. All MLFF schemes increased the k_{nr} values and decrease the PLQY values except in for the $PbBr_3$ models, which showed the opposite trend for the scheme 3 calculations.

4. DISCUSSION

We attempt to identify an optimal duration of the MLFF-MD trajectory to reach an acceptable level of discrepancy between AIMD and MLFF-MD nonadiabatic dynamics. To this end, we performed MLFF-MD using MLFFs trained using an *NPT*, *NVT*, or *NVE* ensemble and examined the MSD of the MLFF-MD trajectory with an AIMD trajectory used as the reference;

https://doi.org/10.1021/acs.jpcc.3c07216
J. Phys. Chem. C 2024, 128, 3935−3944

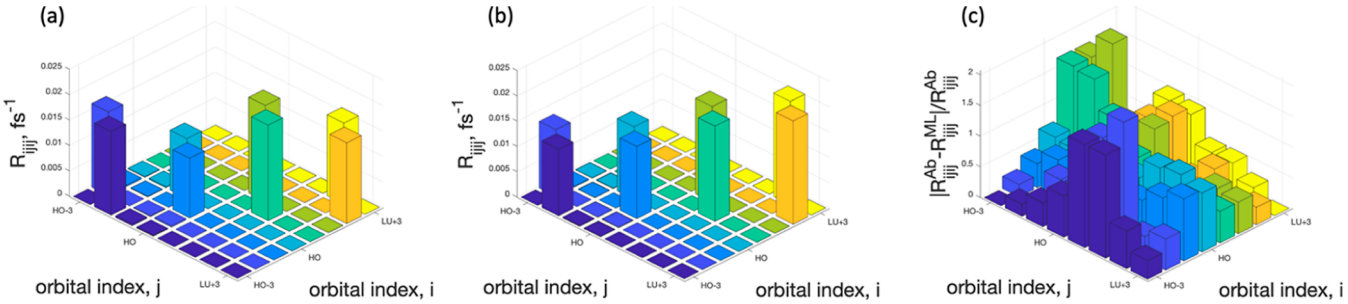

Figure 5. Redfield tensor for n = 3 PbI_3 calculated using NACs determined with (a) AIMD and (b) MLFF-MD method B scheme 1. The R_{iijj} axis represents the nonradiative state to state transition rates. The alternating high intensity transitions near the main diagonal are between near-degenerate states. (c) The relative difference of the Redfield tensor elements shown in (a,b).

Table 3. Oscillator Strength f_{ij} (eq 5) and Energy Dissipation Rates k_e and k_h (eq 22) for Different Excitations[a]

model	transition	f_{ij}	*NVE* MD method	k_e[b] [ps^{-1}]	k_h[b] [ps^{-1}]	k_e[c] [ps^{-1}]	k_h[c] [ps^{-1}]
n = 2 $PbBr_3$	HO − 6−LU + 12	1.4649	Ab Initio	0.6544	0.6341		
			scheme 1	0.4566	0.8553	0.5231	0.6764
			scheme 2	12.7519	13.0159	10.7705	12.0429
			scheme 3	0.4740	0.6687	0.3984	0.4040
n = 2 $PbCl_3$	HO − 3−LU + 3	3.7824	Ab Initio	0.6180	0.9301		
			scheme 1	0.4944	0.7888	2.2916	2.2835
			scheme 2	12.2832	14.1066	4.2810	4.3127
			scheme 3	0.5655	0.9176	0.6905	1.0739
n = 3 PbI_3	HO − 13−LU + 7	0.4654	Ab Initio	0.6695	0.5637		
			scheme 1	0.4253	0.7921	0.7125	0.6522
			scheme 2	5.1895	3.8544	6.3425	5.5383
			scheme 3	0.6811	0.6353	0.8572	0.6689
n = 5 $PbCl_3$	HO − 9−LU + 17	3.6709	Ab Initio	0.4174	0.7319		
			scheme 1	0.6397	1.7498	0.5169	0.9091
			scheme 2	9.2751	8.7018	8.6343	8.2687
			scheme 3	0.5989	0.7273	0.6490	0.8005

[a]The initial conditions represent the highest oscillator strength excitation that does not involve one of the near-degenerate principal band gap orbitals. [b]Nonadiabatic dynamics calculated using MLFF-MD method A trajectory for schemes 1, 2, and 3. [c]Nonadiabatic dynamics calculated using MLFF-MD method B trajectory for schemes 1, 2, and 3.

Table 4. Oscillator Strength f_{ij} (eq 5) of HO−LU Transition, Radiative Recombination Rate k_r (eq 23), Nonradiative Recombination Rate k_{nr} (eq 18), and Resultant PLQYs (eq 24)

model	f_{ij}	k_r [ps^{-1}]	*NVE* MD method	k_{nr}[a] [ps^{-1}]	PLQY[a]	k_{nr}[b] [ps^{-1}]	PLQY[b]
n = 2 $PbBr_3$	0.7922	1.77×10^{-3}	Ab Initio	1.65×10^{-3}	0.4671		
			scheme 1	8.64×10^{-4}	0.6090	5.01×10^{-4}	0.7188
			scheme 2	5.8331	2.5×10^{-4}	6.8267	2.5×10^{-4}
			scheme 3	2.12×10^{-2}	0.0777	4.04×10^{-2}	0.0448
n = 2 $PbCl_3$	0.0243	3.66×10^{-3}	Ab Initio	2.03×10^{-3}	0.4059		
			scheme 1	1.27×10^{-2}	0.1988	3.99×10^{-1}	0.0137
			scheme 2	4.1671	8.8×10^{-4}	1.9012	2.0×10^{-3}
			scheme 3	1.44×10^{-3}	0.4389	2.93×10^{-3}	0.3652
n = 3 PbI_3	1.0818	8.60×10^{-4}	Ab Initio	2.46×10^{-4}	0.6657		
			scheme 1	1.79×10^{-3}	0.2861	4.59×10^{-4}	0.5458
			scheme 2	1.9769	4.2×10^{-4}	3.4046	2.4×10^{-4}
			scheme 3	7.39×10^{-4}	0.4536	1.50×10^{-3}	0.3138
n = 5 $PbCl_3$	0.0263	3.32×10^{-3}	Ab Initio	2.61×10^{-3}	0.4369		
			scheme 1	6.80×10^{-1}	4.9×10^{-3}	1.26×10^{-2}	0.1831
			scheme 2	3.1718	1.1×10^{-3}	3.2358	1.0×10^{-3}
			scheme 3	5.48×10^{-3}	0.3104	3.75×10^{-3}	0.3726

[a]Nonadiabatic dynamics calculated using MLFF-MD method A trajectory for schemes 1, 2, and 3. [b]Nonadiabatic dynamics calculated using MLFF-MD method B trajectory for schemes 1, 2, and 3.

due to this, we limit the focus of this work to time scales that are achievable by AIMD. We found that the MSD exhibits acceptable levels of error in the early portions of the trajectory but begins to perform worse as the trajectory is allowed to continue. We are attributing this to small numerical instability, while within acceptable limits at small time frames, that causes

https://doi.org/10.1021/acs.jpcc.3c07216
J. Phys. Chem. C 2024, 128, 3935−3944

accumulation of error at longer times. This drives the atomistic configurations away from the primary domain of the phase space where the MLFF was trained. Continuing the dynamics in this region of phase space where the model was not trained increases the numerical error and leads to the increase in temperatures that was seen for scheme 1 MLFF-MD calculations. We also observe this affect for both the scheme 1 and scheme 3 MLFF-MD calculations for the $PbBr_3$ model however here we see this effect due to the increase in thickness of the perovskite layer to $n = 2$ that adds a new layer of cesium to the $PbBr_3$ model in comparison to the $n = 1$ $PbBr_3$ model that was used during the training of the MLFFs resulting in both the scheme 1 and scheme 3 MLFF-MD temperatures and MSDs to rise above acceptable levels. In general, scheme 3 performed better than scheme 1; however, we attribute this to the region of phase space that we were most interested in being well covered by the scheme 3 MLFF. Expanding to regions that we did not focus on in this work should increase the level of error while using the scheme 3 MLFF..

This effect is most noticeable in scheme 2 MLFF-MD calculations. For these calculations, we observe a rapid increase in both temperature and MSD in addition to nonadiabatic dynamics results that differ by orders of magnitude from the AIMD nonadiabatic dynamics. We attribute this to a flaw in the design of the MLFF that was used to perform the scheme 2 calculations. To generate this MLFF, a Nose−Hoover thermostat[53] was used for the *NVT* ensemble calculation that performed the on-the-fly training. Choosing the Langevin thermostat[54] would likely provide better results due to its stochastic nature.

The analysis of the vibrational modes shows that there is a good qualitative agreement between the normal-mode frequencies when they are determined using ab initio or MLFF calculations. Which if further highlighted by the RMSE of less than 0.2 for all MLFF calculations, indicating little deviation between the vibrational modes determined by the different calculations. We do however see that there is variation in the normal-mode frequencies that are attributed to C−H stretching modes. This variation likely has little effect on the nonadiabatic dynamics that we are most interested in here due to the poor orbital overlap of the Pb^{2+} and X^- ions with the NH_3^+ functional groups.[36,55] However, this variation could be decreased by decreasing the time step used during the AIMD while performing the on-the-fly training of the MLFF.

This approach aims to reproduce the potential energy surface for the ground state of periodic crystalline surfaces with a dynamic reconstruction of the surface. It establishes a trained correlation between structures and potential energy as a tool for subsequent computations of gradients and forces based on the obtained potential energy without further DFT. Translation invariance is expected to be allowed for integer numbers along the lattice unit vectors along directions orthogonal to exposed surfaces, while rotational invariance is allowed only for discrete rotation dictated by the symmetry group of the crystal.

5. CONCLUSIONS

Here, we explored the expansion of Redfield theory using "on-the-fly" calculated nonadiabatic couplings[34,56,57] to determine excited-state dynamics of materials to work with machine learning force-fields molecular dynamics. To this end, we generated a machine learned force-field using lead halide perovskite models in canonical, microcanonical, and isothermal−isobaric ensembles and performed MD using both MLFFs and an ab initio calculation. Nonadiabatic couplings were then determined for both the MLFF-MD and ab initio MD trajectories, and excited-state dynamics were calculated to determine the influence of the MLFFs on the calculations. We compare MLFF and ab initio calculations in terms of (1) mean squared displacement, (2) role of thermostat in *NVT* training on MLFF, (3) choice of models used for MLFF training, (4) energy dissipation rates and photoluminescence properties, and (5) density of vibrational modes.

(1) MSD calculations show that the MLFF calculate the MD trajectory within the expectations that one could be expected to obtain while using an ab initio calculation. While this is true for all MLFFs, we find that the MLFFs trained in different ensembles result in a large difference in temperature of the resulting MD calculation. MLFFs trained in a *NVT* ensemble show a large increase in temperature that is not seen when using MLFFs trained in a *NPT* or *NVE* ensemble. The temperature and MSD calculations show that numerical instability in the calculations can result in configurations away from the phase space where the MLFFs were trained.

(2) Temperature, MSD, and SKSO energy fluctuations show that the calculations using the *NVT* trained MLFF show instabilities that quickly result in large increases in temperature and MSD. While the SKSO energies quickly move together resulting in a single band. Using the Langevin thermostat while training the MLFF should reduce the amount of error observed.

(3) Temperature, MSD, and SKSO energy fluctuations show that the choice of models when training has an effect of the outcome of the MLFF-MD calculations. This is most noticeable in the $PbBr_3$ case where a $n = 1$ model was used to train the MLFFs while an $n = 2$ model was used to test the MLFFs. The $PbBr_3$ model shows the most rapid deviation from the ab initio for MSD and temperature for the *NPT* trained MLffs and is the only model to show a significant deviation for *NVE* trained MLFFs. This is likely due to the addition of a Cs/Br layer in the model when n increase to two which is not present in the $PbBr_3$ model that was used for training.

(4) The nonadiabatic dynamics using both the *NPT* and *NVE* trained MLFFs for MLFF-MD showed similar results to each other and to the results obtained using AIMD. Producing an MLFF that uses both and *NVE* and *NPT* ensemble during training may further increase the accuracy of the results due to the larger coverage of phase space obtained by the *NPT* ensemble and the greater coverage of the region that we are interested in by the *NVE* ensemble. Reducing the temperature ramping during the on-the-fly learning to a temperature range that is of interest for the material should also result in a greater coverage of the phase space of interest.

(5) The vibrational modes showed good qualitative agreement between all calculation methods and a small RMSE between the MLFF and ab initio calculations. However, there is variation among the normal modes that are attributed to the stretching between carbon and hydrogen. Further work should be performed to improve the qualitative agreement for these normal modes.

Areas of continued interest that require further work would be to examine the limits of this method as we increase the time scale of the calculation beyond those allowed by ab initio

https://doi.org/10.1021/acs.jpcc.3c07216
J. Phys. Chem. C 2024, 128, 3935−3944

molecular dynamics and to determine the effectiveness of MLFF-MD when used for excited-state nonadiabatic dynamics simulations using atomistic models that include charge injection or when an excited-stated potential energy surface is used to account for changes due to an excitation.

■ ASSOCIATED CONTENT

Supporting Information

The Supporting Information is available free of charge at https://pubs.acs.org/doi/10.1021/acs.jpcc.3c07216.

Illustration of the atomistic models of used; expanded figure of calculated temperature showing scheme 2 results; SKSO energy fluctuations using MLFF-MD methods A and B for $n = 2$ $PbBr_3$, $n = 2$ $PbCl_3$, and $n = 3$ PbI_3 models; SKSO energy fluctuations using MLFF-MD method A $n = 2$ $PbCl_3$ model; Redfield tensor for $n = 3$ PbI_3 for ab inito, MLFF-MD methods A and B for scheme 3, and MLFF-MD method A for scheme 1; root mean square error of Redfield tensor; and transition, oscillator strength, and energy dissipations rates for the second and third highest oscillator strength transitions (PDF)

■ AUTHOR INFORMATION

Corresponding Author

Dmitri S. Kilin − *Department of Chemistry and Biochemistry, North Dakota State University, Fargo, North Dakota 58108, United States;* orcid.org/0000-0001-7847-5549; Email: dmitri.kilin@ndsu.edu

Author

David R. Graupner − *Department of Chemistry and Biochemistry, North Dakota State University, Fargo, North Dakota 58108, United States;* orcid.org/0000-0003-3879-8559

Complete contact information is available at: https://pubs.acs.org/10.1021/acs.jpcc.3c07216

Notes

The authors declare no competing financial interest.

■ ACKNOWLEDGMENTS

D.R.G. thanks NSF CHE- 2004197 for the exploration of interfacial phenomena in semiconductor nanostructures. D.S.K. thanks NSF CHE—1944921 for support of quantum dynamics research. This research used resources of the National Energy Research Scientific Computing Center (NERSC), a U.S. Department of Energy Office of Science User Facility located at Lawrence Berkeley National Laboratory, operated under contract no. DE-AC02-05CH11231 using allocation award m1251 for 2023, "Computational Modeling of Photo-catalysis and Photo-induced Charge Transfer Dynamics on Surfaces". This work used resources of the Center for Computationally Assisted Science and Technology (CCAST) at North Dakota State University, which were made possible in part by NSF MRI award no. 2019077. D.K. thanks Sergei Tretiak, Oleg Prezhdo, David Micha, Bakhtiyor Rasulev, and Svetlana Kilina for inspiring discussions. We also thank Nikita Fedik, Aaron Forde, Yulun Han, Landon Johnson, Steven Westra, Dinesh Thapa, William Tupa, Grace Tiffany, Spencer Gilman, and Wyatt Wilcox for collective discussion and editing.

■ REFERENCES

(1) Arabpour Roghabadi, F.; Alidaei, M.; Mousavi, S. M.; Ashjari, T.; Tehrani, A. S.; Ahmadi, V.; Sadrameli, S. M. Stability progress of perovskite solar cells dependent on the crystalline structure: From 3D ABX3 to 2D Ruddlesden-Popper perovskite absorbers. *J. Mater. Chem. A* **2019**, *7* (11), 5898−5933.

(2) Protesescu, L.; Yakunin, S.; Bodnarchuk, M. I.; Krieg, F.; Caputo, R.; Hendon, C. H.; Yang, R. X.; Walsh, A.; Kovalenko, M. V. Nanocrystals of Cesium Lead Halide Perovskites (CsPbX3, X = Cl, Br, and I): Novel Optoelectronic Materials Showing Bright Emission with Wide Color Gamut. *Nano Lett.* **2015**, *15* (6), 3692−3696.

(3) Koh, T. M.; Shanmugam, V.; Schlipf, J.; Oesinghaus, L.; Muller-Buschbaum, P.; Ramakrishnan, N.; Swamy, V.; Mathews, N.; Boix, P. P.; Mhaisalkar, S. G. Nanostructuring Mixed-Dimensional Perovskites: A Route Toward Tunable, Efficient Photovoltaics. *Adv. Mater.* **2016**, *28* (19), 3653−3661.

(4) Dong, H.; Ran, C.; Gao, W.; Li, M.; Xia, Y.; Huang, W. Metal Halide Perovskite for next-generation optoelectronics: progresses and prospects. *eLight* **2023**, *3* (1), 3.

(5) Esch, M. P.; Shu, Y.; Levine, B. G. A Conical Intersection Perspective on the Low Nonradiative Recombination Rate in Lead Halide Perovskites. *J. Phys. Chem. A* **2019**, *123* (13), 2661−2673.

(6) Nie, W.; Tsai, H.; Asadpour, R.; Blancon, J.-C.; Neukirch, A. J.; Gupta, G.; Crochet, J. J.; Chhowalla, M.; Tretiak, S.; Alam, M. A.; et al. High-efficiency solution-processed perovskite solar cells with millimeter-scale grains. *Science* **2015**, *347* (6221), 522−525.

(7) Yang, L.; Wang, X.; Mai, X.; Wang, T.; Wang, C.; Li, X.; Murugadoss, V.; Shao, Q.; Angaiah, S.; Guo, Z. Constructing efficient mixed-ion perovskite solar cells based on TiO2 nanorod array. *J. Colloid Interface Sci.* **2019**, *534*, 459−468.

(8) Huang, Y.; Yuan, Z.; Yang, J.; Yin, S.; Liang, A.; Xie, G.; Feng, C.; Zhou, Z.; Xue, Q.; Pan, Y.; et al. Highly efficient perovskite solar cells by building 2D/3D perovskite heterojuction in situ for interfacial passivation and energy level adjustment. *Sci. China: Chem.* **2023**, *66* (2), 449−458.

(9) Song, J.; Li, J.; Li, X.; Xu, L.; Dong, Y.; Zeng, H. Quantum Dot Light-Emitting Diodes Based on Inorganic Perovskite Cesium Lead Halides (CsPbX3). *Adv. Mater.* **2015**, *27* (44), 7162−7167.

(10) Lin, K.; Xing, J.; Quan, L. N.; de Arquer, F. P. G.; Gong, X.; Lu, J.; Xie, L.; Zhao, W.; Zhang, D.; Yan, C.; et al. Perovskite light-emitting diodes with external quantum efficiency exceeding 20 per cent. *Nature* **2018**, *562* (7726), 245−248.

(11) Park, M. H. 3D and 2D Metal Halide Perovskites for Blue Light-Emitting Diodes. *Materials* **2022**, *15* (13), 4571.

(12) Leung, T. L.; Ahmad, I.; Syed, A. A.; Ng, A. M. C.; Popović, J.; Djurišić, A. B. Stability of 2D and quasi-2D perovskite materials and devices. *Commun. Mater.* **2022**, *3* (1), 63.

(13) Ghosh, D.; Neukirch, A. J.; Tretiak, S. Optoelectronic Properties of Two-Dimensional Bromide Perovskites: Influences of Spacer Cations. *J. Phys. Chem. Lett.* **2020**, *11* (8), 2955−2964.

(14) Wang, K.; Park, J. Y.; Akriti; Dou, L. Two-dimensional halide perovskite quantum-well emitters: A critical review. *EcoMat* **2021**, *3* (3), No. e12104.

(15) Stoumpos, C. C.; Cao, D. H.; Clark, D. J.; Young, J.; Rondinelli, J. M.; Jang, J. I.; Hupp, J. T.; Kanatzidis, M. G. Ruddlesden-Popper Hybrid Lead Iodide Perovskite 2D Homologous Semiconductors. *Chem. Mater.* **2016**, *28* (8), 2852−2867.

(16) Dion, M.; Ganne, M.; Tournoux, M. Nouvelles familles de phases MIMII2Nb3O10 a feuillets "perovskites. *Mater. Res. Bull.* **1981**, *16* (11), 1429−1435.

(17) Jacobson, A. J.; Johnson, J. W.; Lewandowski, J. T. Interlayer chemistry between thick transition-metal oxide layers: synthesis and intercalation reactions of K[Ca2Nan-3NbnO3n+1] ($3 \leq n \leq 7$). *Inorg. Chem.* **1985**, *24* (23), 3727−3729.

(18) Li, X.; Lubbers, N.; Tretiak, S.; Barros, K.; Zhang, Y. Machine Learning Framework for Modeling Exciton-Polaritons in Molecular Materials. *arXiv* **2023**, arXiv:2306.02523v3.

(19) Matin, S.; Allen, A.; Smith, J. S.; Lubbers, N.; Jadrich, R. B.; Messerly, R. A.; Nebgen, B. T.; Li, Y. W.; Tretiak, S.; Barros, K.

Machine learning potentials with Iterative Boltzmann Inversion: training to experiment. *arXiv* **2023**, arXiv:2307.04712v1.
(20) Wang, B.; Wu, Y.; Liu, D.; Vasenko, A. S.; Casanova, D.; Prezhdo, O. V. Efficient Modeling of Quantum Dynamics of Charge Carriers in Materials Using Short Nonequilibrium Molecular Dynamics. *J. Phys. Chem. Lett.* **2023**, *14* (37), 8289−8295.
(21) Wang, B.; Winkler, L.; Wu, Y.; Müller, K. R.; Sauceda, H. E.; Prezhdo, O. V. Interpolating Nonadiabatic Molecular Dynamics Hamiltonian with Bidirectional Long Short-Term Memory Networks. *J. Phys. Chem. Lett.* **2023**, *14* (31), 7092−7099.
(22) Jinnouchi, R.; Lahnsteiner, J.; Karsai, F.; Kresse, G.; Bokdam, M. Phase Transitions of Hybrid Perovskites Simulated by Machine-Learning Force Fields Trained on the Fly with Bayesian Inference. *Phys. Rev. Lett.* **2019**, *122* (22), 225701.
(23) Mishin, Y. Machine-learning interatomic potentials for materials science. *Acta Mater.* **2021**, *214*, 116980.
(24) Jinnouchi, R.; Karsai, F.; Kresse, G. On-the-fly machine learning force field generation: Application to melting points. *Phys. Rev. B* **2019**, *100* (1), 014105.
(25) Jinnouchi, R.; Karsai, F.; Kresse, G. Making free-energy calculations routine: Combining first principles with machine learning. *Phys. Rev. B* **2020**, *101* (6), 060201.
(26) Jinnouchi, R.; Miwa, K.; Karsai, F.; Kresse, G.; Asahi, R. On-the-Fly Active Learning of Interatomic Potentials for Large-Scale Atomistic Simulations. *J. Phys. Chem. Lett.* **2020**, *11* (17), 6946−6955.
(27) Webb, S. P.; Iordanov, T.; Hammes-Schiffer, S. Multiconfigurational nuclear-electronic orbital approach: Incorporation of nuclear quantum effects in electronic structure calculations. *J. Chem. Phys.* **2002**, *117* (9), 4106−4118.
(28) Hammes-Schiffer, S.; Tully, J. C. Proton transfer in solution: Molecular dynamics with quantum transitions. *J. Chem. Phys.* **1994**, *101* (6), 4657−4667.
(29) Kryjevski, A.; Mihaylov, D.; Kilina, S.; Kilin, D. Multiple exciton generation in chiral carbon nanotubes: Density functional theory based computation. *J. Chem. Phys.* **2017**, *147* (15), 154106.
(30) Tully, J. C. Molecular dynamics with electronic transitions. *J. Chem. Phys.* **1990**, *93* (2), 1061−1071.
(31) Redfield, A. G. On the Theory of Relaxation Processes. *IBM J. Res. Dev.* **1957**, *1*, 19−31.
(32) Vazhappilly, T.; Micha, D. A. Computational Modeling of the Dielectric Function of Silicon Slabs with Varying Thickness. *J. Phys. Chem. C* **2014**, *118* (8), 4429−4436.
(33) Kilina, S.; Kilin, D.; Tretiak, S. Light-Driven and Phonon-Assisted Dynamics in Organic and Semiconductor Nanostructures. *Chem. Rev.* **2015**, *115* (12), 5929−5978.
(34) Huang, S.; Kilin, D. S. Charge Transfer, Luminescence, and Phonon Bottleneck in TiO2 Nanowires Computed by Eigenvectors of Liouville Superoperator. *J. Chem. Theory Comput.* **2014**, *10* (9), 3996−4005.
(35) Jean, J. M.; Friesner, R. A.; Fleming, G. R. Application of a multilevel Redfield theory to electron transfer in condensed phases. *J. Chem. Phys.* **1992**, *96* (8), 5827−5842.
(36) Forde, A.; Inerbaev, T.; Hobbie, E. K.; Kilin, D. S. Excited-State Dynamics of a CsPbBr3 Nanocrystal Terminated with Binary Ligands: Sparse Density of States with Giant Spin-Orbit Coupling Suppresses Carrier Cooling. *J. Am. Chem. Soc.* **2019**, *141* (10), 4388−4397.
(37) Graupner, D. R.; Kilin, D. S. Effect of Stacking 2D Lead Chloride Perovskites into Vertical Heterostructures on Photoluminescence Intensity. *J. Appl. Spectrosc.* **2023**, *90* (2), 436−447.
(38) Kubler, J.; Hock, K. H.; Sticht, J.; Williams, A. R. Density functional theory of non-collinear magnetism. *J. Phys. F: Met. Phys.* **1988**, *18* (3), 469−483.
(39) Barth, U. v.; Hedin, L. A local exchange-correlation potential for the spin polarized case. i. *J. Phys. C: Solid State Phys.* **1972**, *5* (13), 1629−1642.
(40) Vogel, D. J.; Kilin, D. S. First-Principles Treatment of Photoluminescence in Semiconductors. *J. Phys. Chem. C* **2015**, *119* (50), 27954−27964.
(41) Han, Y.; Meng, Q.; Rasulev, B.; May, P. S.; Berry, M. T.; Kilin, D. S. Photoinduced Charge Transfer versus Fragmentation Pathways in Lanthanum Cyclopentadienyl Complexes. *J. Chem. Theory Comput.* **2017**, *13* (9), 4281−4296.
(42) Bartók, A. P.; Kondor, R.; Csányi, G. On representing chemical environments. *Phys. Rev. B* **2013**, *87* (18), 184115.
(43) Bartók, A. P.; Payne, M. C.; Kondor, R.; Csányi, G. Gaussian Approximation Potentials: The Accuracy of Quantum Mechanics, without the Electrons. *Phys. Rev. Lett.* **2010**, *104* (13), 136403.
(44) Jinnouchi, R.; Karsai, F.; Verdi, C.; Asahi, R.; Kresse, G. Descriptors representing two- and three-body atomic distributions and their effects on the accuracy of machine-learned inter-atomic potentials. *J. Chem. Phys.* **2020**, *152* (23), 234102.
(45) Redfield, A. G. On the Theory of Relaxation Processes. *IBM J. Res. Dev.* **1957**, *1* (1), 19−31.
(46) Einstein, A. On the Quantum theory of radiation. *Phys. Z.* **1917**, *18*, 121−128.
(47) Graupner, D. R.; Kilin, D. S. Role of heterostacking of 2D lead chloride perovskites on photoluminescence. *MRS Adv.* **2022**, *7* (30), 772−777.
(48) Graupner, D. R.; Kilin, D. Role of perovskite thickness on optoelectronic properties in lead bromide and lead iodide thin film perovskites: A DFT study. *MRS Adv.* **2023**, *8* (16), 901−906.
(49) Kresse, G.; Joubert, D. From ultrasoft pseudopotentials to the projector augmented-wave method. *Phys. Rev. B* **1999**, *59* (3), 1758−1775.
(50) Blöchl, P. E. Projector augmented-wave method. *Phys. Rev. B* **1994**, *50* (24), 17953−17979.
(51) Perdew, J. P.; Burke, K.; Ernzerhof, M. Generalized Gradient Approximation Made Simple [Phys. Rev. Lett. 77, 3865 (1996)]. *Phys. Rev. Lett.* **1997**, *78* (7), 1396.
(52) Kresse, G.; Furthmüller, J. Efficiency of ab-initio total energy calculations for metals and semiconductors using a plane-wave basis set. *Comput. Mater. Sci.* **1996**, *6* (1), 15−50.
(53) Nosé, S. A unified formulation of the constant temperature molecular dynamics methods. *J. Chem. Phys.* **1984**, *81* (1), 511−519.
(54) Hoover, W. G.; Ladd, A. J. C.; Moran, B. High-Strain-Rate Plastic Flow Studied via Nonequilibrium Molecular Dynamics. *Phys. Rev. Lett.* **1982**, *48* (26), 1818−1820.
(55) Forde, A.; Inerbaev, T.; Kilin, D. Spectral Signatures of Positive and Negative Polarons in Lead-Halide Perovskite Nanocrystals. *J. Phys. Chem. C* **2020**, *124* (1), 1027−1041.
(56) Han, Y.; Vogel, D. J.; Inerbaev, T. M.; May, P. S.; Berry, M. T.; Kilin, D. S. Photoinduced dynamics to photoluminescence in Ln^{3+} (Ln = Ce, Pr) doped β-$NaYF_4$ nanocrystals computed in basis of non-collinear spin DFT with spin-orbit coupling. *Mol. Phys.* **2018**, *116* (5−6), 697−707.
(57) Kilin, D. S.; Micha, D. A. Relaxation of Photoexcited Electrons at a Nanostructured Si(111) Surface. *J. Phys. Chem. Lett.* **2010**, *1* (7), 1073−1077.

https://doi.org/10.1021/acs.jpcc.3c07216
J. Phys. Chem. C 2024, 128, 3935−3944